ADVANCED FUNCTIONAL MATERIALS
www.afm-journal.de

Engineering Route for Stretchable, 3D Microarchitectures of Wide Bandgap Semiconductors for Biomedical Applications

Thanh-An Truong, Tuan Khoa Nguyen, Xinghao Huang, Aditya Ashok, Sharda Yadav, Yoonseok Park, Mai Thanh Thai, Nhat-Khuong Nguyen, Hedieh Fallahi, Shuhua Peng, Sima Dimitrijev, Yi-Chin Toh, Yusuke Yamauchi, Chun Hui Wang, Nigel Hamilton Lovell, John Ashley Rogers, Thanh Nho Do, Nam-Trung Nguyen, Hangbo Zhao, and Hoang-Phuong Phan**

Wide bandgap (WBG) semiconductors have attracted significant research interest for the development of a broad range of flexible electronic applications, including wearable sensors, soft logical circuits, and long-term implanted neuromodulators. Conventionally, these materials are grown on standard silicon substrates, and then transferred onto soft polymers using mechanical stamping processes. This technique can retain the excellent electrical properties of wide bandgap materials after transfer and enables flexibility; however, most devices are constrained by 2D configurations that exhibit limited mechanical stretchability and morphologies compared with 3D biological systems. Herein, a stamping-free micromachining process is presented to realize, for the first time, 3D flexible and stretchable wide bandgap electronics. The approach applies photolithography on both sides of free-standing nanomembranes, which enables the formation of flexible architectures directly on standard silicon wafers to tailor the optical transparency and mechanical properties of the material. Subsequent detachment of the flexible devices from the support substrate and controlled mechanical buckling transforms the 2D precursors of wide band gap semiconductors into complex 3D mesoscale structures. The ability to fabricate wide band gap materials with 3D architectures that offer device-level stretchability combined with their multi-modal sensing capability will greatly facilitate the establishment of advanced 3D bio-electronics interfaces.

1. Introduction

Flexible and stretchable electronic systems represent a new class of semiconductor devices with great potential for biomedical applications because of the close match of mechanical properties with those of human skin.[1–6] These devices are realized through the integration of functional semiconductor nanomembranes with soft flexible substrates, such as silicone elastomers and hydrogels, and thus offer an intimate, conformal interface with biological tissues. Thin, soft, skin-like epidermal electronics systems have been shown to be capable of performing precise and continuous recording of multiple biometric signals, including temperature,[7] mechano-acoustic signals,[8–10] electrophysiological signals such as electromyography (EMG) and electroencephalography (EEG),[11] and sweat biomarkers.[12,13] Flexible electronics [14] have also been utilized in various implanted sensing and stimulating platforms, such as transcranial optogenetic and wireless optogenetics,[15–21]

T.-A. Truong, S. Peng, C. H. Wang, H.-P. Phan
School of Mechanical and Manufacturing Engineering
The University of New South Wales
Sydney, NSW 2052, Australia
E-mail: hp.phan@unsw.edu.au

T. K. Nguyen, S. Yadav, N.-K. Nguyen, H. Fallahi, S. Dimitrijev, N.-T. Nguyen
Queensland Micro and Nanotechnology Centre
Griffith University
Nathan, QLD 4111, Australia

The ORCID identification number(s) for the author(s) of this article can be found under https://doi.org/10.1002/adfm.202211781.

DOI: 10.1002/adfm.202211781

X. Huang, H. Zhao
Department of Aerospace and Mechanical Engineering
University of Southern California
Los Angeles, CA 90089, USA
E-mail: hangbozh@usc.edu

A. Ashok, Y. Yamauchi
Australian Institute for Bioengineering and Nanotechnology
The University of Queensland
Brisbane, QLD 4072, Australia

Y. Park
Department of Advanced Materials Engineering for Information and Electronics
Kyung Hee University
Yongin 17104, Republic of Korea

M. T. Thai, N. H. Lovell, T. N. Do
Graduate School of Biomedical Engineering
University of New South Wales
Sydney, NSW 2052, Australia

peripheral nerve coolers [22] and stimulators,[23] as well as cardiac pacemakers.[24] The implementation of these soft wearable or implantable biomedical applications offers unprecedented functionalities and capabilities, which are expected to revolutionize the quality of health monitoring, diagnosis, and therapy.

Silicon nanomembranes (Si NMs) are the mainstream semiconducting material used to build functional and flexible bioelectronic components due to their excellent electronic properties (e.g., high electron mobilities, and significant sensing phenomena), abundance on earth, together with a mature manufacturing technology of silicon. The transfer printing process of Si NMS coupled with controlled mechanical buckling establishes a route to engineer unique 3D mesostructures with exciting functionalities, such as 3D bioelectronic interfaces. Compared to 2D membrane devices, 3D architectures can impart device-level stretchability while avoiding material fracture commonly associated with 2D inorganic nanomembranes. These mesoscale 3D structures also provide geometries that conform to bioengineered 3D human tissue models, such as spheroids, organoids, and assembloids, which underpin fundamental investigation into neurodevelopment, evolution and origin of diseases, and drug screening.[25] Therefore, there is increasing interest to embed electronic strain and temperature sensors alongside electrophysiological recording electrodes into 3D electronic sensing construct to monitor various electrophysiological signals in the human body, ranging from contractile forces of cardiac-and musculoskeletal tissues[26] to neural signaling during healthy and injured states.[27]

However, the translation of Si-based 3D mesostructures as a flexible bioelectronic interface in implants or *ex vivo* tissues is hampered by Si's high reactivity to water (i.e., hydrolysis). This results in the degradation of the functional bioelectronic layer over long-term use under aqueous conditions within the body or in tissue cultures. In addition to biodegradation, Si material exhibits a small energy gap, resulting in high absorption at visible wavelengths. This intrinsic optical property can potentially limit the application of Si in transparent optoelectronics, which require simultaneous electrophysiological measurement and optical mapping. Compared to Si,WBG semiconductors, such as silicon carbide (SiC), gallium nitride (GaN), and diamond, have strong covalent bonds between their atoms and exhibit excellent transparency in the visible light wavelength range. They have emerged as promising candidates to develop multi-modal biosystems, including neural stimulation electrodes, implanted light-emitting diodes (LED), and glucose sensors.[28] Nonetheless, it has been challenging to fabricate flexible devices from WBG materials due to their large Young's modulus, which results in a high bending stiffness in the bulk material form. Recent advancement in the synthesis and growth processes of nanoscale thin film WBG materials and the development of transfer printing processes open exciting opportunities in the fabrication of flexible WBG electronics systems. For instance, the use of a sacrificial ZnO layer enables lifting-off GaN-based LED from the traditional rigid sapphire substrate,[29,30] thereby expanding the practical applications of III-nitride systems to flexible optoelectronics. The chemical lift-off process was also utilized to form soft AlGaN/GaN high electron mobility transistors with comparable drain current to that of the rigid devices, establishing a viable design approach for wearable logic circuits.[31,32] Doped SiC nanomembranes grown on silicon wafers and then mechanically stamped onto polyimide films exhibited excellent electrical stability in biofluids, demonstrating great potential for long-term implanted neuromodulators. Although significant progress has been made in transfer printing methods for soft WBG systems, state-of-the-art technologies are still limited to stamping planar 2D nanomembranes. Moreover, they typically require a sacrificial layer to facilitate the detachment of these semiconductors from the support substrate. These manufacturing constraints have so far limited the development of 3D WBG electronic systems with complex geometries that are imperative in stretchable, shrinkable electronics, as well as 3D bioelectronic interface applications.

Taking advantage of the optical transparency and mechanical robustness of WBG semiconductors, this work presents a new engineering approach to create soft, 3D mesostructured WBG materials that eliminates the need for a sacrificial layer. We demonstrate this fabrication concept on a SiC-on-Si platform by applying a lithography process on both sides of a few hundred-nanometer-thick, free-standing nanomembranes. This allowed the exposure of the underlying photoresist through the transparent SiC membranes, thereby eliminating the large distance between the photomask and the resist layer in the conventional Si microcavity approach. The optical transparency of the SiC membrane allowed the stacking and patterning of different materials, such as polyimide microstructures and metallic paths, on both sides of the membrane. The combination of these features enabled the fabrication of scalable flexible WBG electronics on standard Si platforms without relying on traditional mechanical stamping processes, which require multiple additional steps and risk of damage during transferring. The paper also validates the versatility of our technique by successfully demonstrating the backside fabrication process on other wide-bandgap and ultra-wide-bandgap materials, such as GaN (with a bandgap of 3.4 eV) and SiN (with a bandgap of ≈5.8 eV).

2. Results and Discussion

2.1. Fabrication Process on Free-Standing Membranes

Figure 1 illustrates the process to transform rigid SiC membranes deposited on a Si substrate into flexible multimodal 3D

Y.-C. Toh
School of Mechanical
Medical and Process Engineering
Queensland University of Technology
Brisbane, QLD 4059, Australia

N. H. Lovell, T. N. Do, H.-P. Phan
Tyree Institute of Health Engineering
University of New South Wales
Sydney, NSW 2052, Australia

J. A. Rogers
Department of Materials Science and Engineering
Department of Mechanical Engineering
Department of Biomedical Engineering
Departments of Electrical and Computer Engineering and Chemistry
and Department of Neurological Surgery
Northwestern University
Evanston, IL 60208, USA

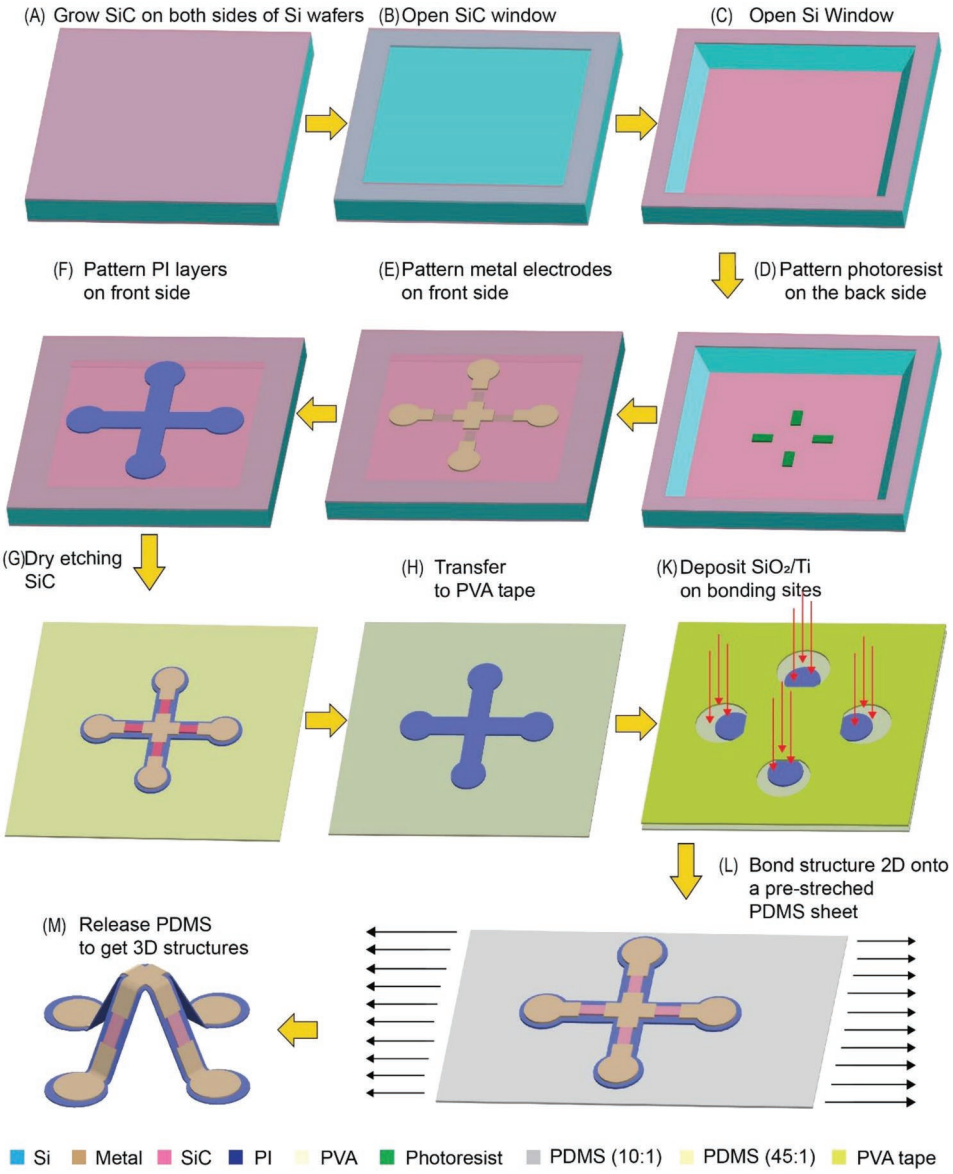

Figure 1. A step by step sketchamic sketch of the engineering route to transform plannar structures into 3D mesostructures. A) Epitaxially grow SiC on both sides of a Si wafer, B) Open SiC window by inductively coupled plasma etching, C) Remove Si in the window by KOH etching, D) Pattern photoresist on the backside, E) Pattern metal contact on the front side, F) Pattern PI on the front side, G) Dry etch SiC after bonding the front side to a sticky PDMS sheet, H) Transfer the 2D mesostructures to a water-soluble tape (PVA), K) Deposit Ti/SiO_2 bonding sites through a shadow mask, L) Bonding 2D mesostructures to a pre-stretched PDMS sheet immediately after air plasma treating, M) Obtain 3D mesostructures by releasing PDMS sheet.

SiC mesostructures. Furhter details are described in the Experimental Section and Supporting Information (Figure S2 and Notes S1 and S2, Supporting Information). Brieftly, the process started with the epitaxial growth of a 3C-SiC nano thin film on a Si substrate. Removal of the Si substrate using wet etching created free-standing, transparent SiC membranes with a 5 mm-wide window. Applying the first step of photolithograpy on the backside of the SiC membranes shaped functional elements such as electrodes, temperature, and strain sensors, for flexible electronic. It should be noted that our approach is well-suited for both maskless and mask-based lithography, making it a versatile techinique for microfabrication. Subsequently, metal (aluminum) and polyimide were deposited and patterned on the front side of the membranes to provide electrical interconect and created 2D precursors of the flexible SiC devices. The 2D soft mesostructures formed on polyimide can be detached from Si substrate by etching away the SiC membranes using inductively coupled plasma etching, while the front side of the membranes is bonded to a stucky PDMS sheet. The 2D structures are transferred to water soluble tape (PVA, Aquasol) to prepare the buckling process. After the deposition of Ti/SiO_2 through shadow masks to create bonding sites, both pre-stretched PDMS sheet and 2D precursors are exposed to air plasma to facilitate the bonding. Once the 2D mesotructures were bonded to pre-stretched PDMS, water soluble tapes were dissolved by emerging the whole setup in warm water. Releasing the pre-stretched PDMS transformed 2D precursors into 3D structures.

2.2. Formation of 2D SiC Structures on Free-Standing Membranes

To validate the feasibility of micropatterning on free-standing SiC membranes, we spin coated AZ5214 photoresist at 4000 rpm on the back side of the nanomembrane and exposed the resist layer through the membrane using a maskless aligner (MLA150) at a wavelength of 405 nm. **Figure 2**A shows a microscopic image of a microgroove photoresist pattern formed on the back side of a SiC nanomembrane. The thickness of the photoresist measured by a step profiler (Bruker Dektak150) was ≈1.7 µm, which was consistent for all microgrooves examined (Figure 2A, left). The results demonstrated that our fabrication method can produce a uniform photoresist thickness and feature with the same quality as those formed on the front side of standard wafers. Figure 2B illustrates different planar microstructures patterned on the back side of the membranes, such as circular arrays, serpentines, Vicsek fractal structures, and Hilbert curves, which are of particular interest for flexible electronics and metamaterial applications.[33] The SEM images also demonstrated the successful fabrication of miniaturized features with a width of less than 8 µm and a sidewall roughness of less than 1 µm, which are not possible using conventional techniques for non-transparent Si microcavities. It was possible to achieve such high resolution with the SiC nanomembranes because the distance between the photomask and the photoresist layer was reduced to the thickness of the nanomembrane (i.e., $s = 200$ nm in equation (1)).

The photoresist micropatterns on the backside served as the hard mark for SiC dry etching to create sensing elements of flexible electronics. Additional layers, such as metal traces, polymeric substrates, and bonding sites (for mechanical buckling), can be introduced from the top side using standard lithography. Due to its optical transparency, all microstructures formed on the SiC membranes in the first step were visible for the subsequent alignment of stacked layers. For instance, the alignment markers for the Aluminium electrode layer on the front side of the SiC membrane were precisely overlaid with those of the photoresist layer on the backside, as illustrated in Figure 2C. The ability to fully process flexible WBG electronics on standard Si wafers is a significant advantage as it eliminates the time-consuming stamping step as well as the need for a temporary hosting substrate prior to release.

Not only limited to 3C-SiC (with a band gap of 2.3 eV), we further extend our simple double-side lithography technique to a wide range of WBG materials that can be directly deposited on a Si substrate. For example, the technique is highly suitable for AlGaN/GaN membranes epitaxially grown on <111> Si wafers (30 nm AlGaN /1.5 µm GaN /1.5 µm buffer sourced from DOWA Electronics Materials Co., Ltd.). Here <111> Si is typically used as the template for the growth of GaN due to the close lattice constant of this crystallographic surface to that of the GaN crystal. As a consequence, to form free standing AlGaN/GaN membranes, wet etching using HNA (Hydrofluoric, Nitric, and Acetic) or dry etching using DRIE can be employed to remove the Si substrate owing to the good etch selectivity of GaN over Si. It is noteworthy to point out that GaN exhibits a cut-off band at 365 nm.[34] Therefore, to make it possible to expose photoresist spincoated on the backside through GaN membranes, we employed a higher exposure source with a wavelength of 405 nm, corresponding to an optical transmittance of ≈80%.[34] Figure 2D (left) shows the optical transparency of AlGaN/GaN, allowing observation of a smartphone RGB pixels through a free-standing membrane. Figure 2D (right) represents several micro features successfully formed on the frontside and backside of AlGaN/GaN membranes with a high quality of alignment.[35–37] To demonstrate the potential of our technology for functional III-Nitride based devices, we employed Cr/Au (10 nm/100 nm) as the electrode for the rectangular-shaped 2DEG resistor. We developed a two-terminal 2DEG AlGaN/GaN resistance with a dimension of 30 um wide 180 um long on a free-standing membrane. The IV characteristic of the 2DEG device shows a high current at an applied voltage of 1V, implying a highly conductive channel formed (200 Ω) at the interface of AlGaN/GaN (i.e., the 2DEG layer) (Figure S5, Supporting Information). These results indicate the promise of our engineering route to form flexible electronics (e.g., LED or High Electron Mobility Transistors) using III-Nitride semiconductors.[35–37]

Further pushing the energy band gap to the insulator range, we showed that our method can also transfer dielectric material (e.g., silicon nitride with a band gap of ≈5.8 eV) on to polymers. Here, SiN free-standing membranes were fabricated using KOH etching of the Si substrate that is similar to the process for SiC membranes. The excellent optical transparency of SiN (with optical transmittance of 90% at the wavelength of 365 nm) enabled the overlaying of complex microlithography structures (e.g., cross, flowers) on both sides, in Figure 2E.

Following the above backside lithography steps, etching away the uncoated SiC areas from the back side helps to release the flexible SiC electronics on a polyimide platform, which had excellent mechanical bendability, as illustrated by its ability to wrap around a water droplet (radius 2 mm) by liquid surface tension (Figure 2F(i)). Complex microstructures, such as micromesh (widely used in physiological recording), where miniaturized SiC electrodes were well centered on a polyimide micronet, can be conveniently obtained via our fabrication approach, suggesting a promising possibility for high density electrode arrays for neural recording and stimulation applications, Figure 2F(i,ii). It should be noted that we mainly employed polyimide (PI) as the constructing substrate for flexible SiC devices in this work due to its ease of fabrication and chemical inertness. However, our technology is also applicable to other polymeric systems, such as PDMS and SU8, where their unique mechanical properties can be tailored for specific applications. For instance, Figure 2F(iii) demonstrates a stamping-free fabrication of serpentine SiC on PDMS that offers excellent bendability (bending radius ≈3 mm) and optical transparency, with potential applications in wearable health monitoring systems.[33]

2.3. Multimodalities of Flexible WBG Systems

2.3.1. Mechanical Flexibility

After releasing SiC-on-polyimide films from the Si substrate, we characterized their mechanical bendability using a setup

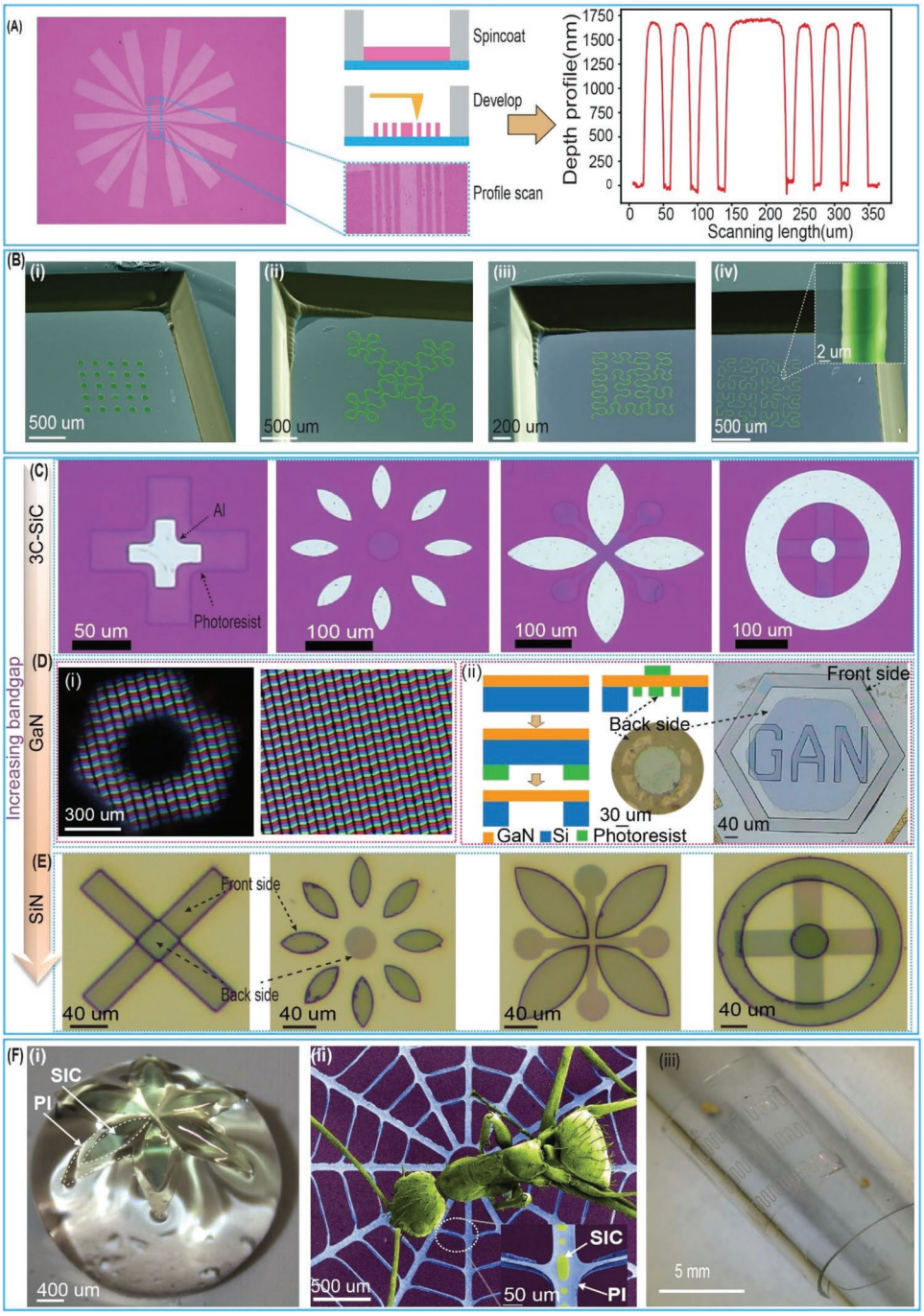

Figure 2. Micro-structures formed by back-side photolithography and double-side photolithography on free-standing SiC nanomembranes. A) Optical images of photoresist patterns on the back side of SiC free-standing membranes (right) and the corresponding step height profile (left), B) SEM images of different photoresist patterns on the back side of SiC free-standing membranes, C) Optical images showing good alignment of photoresist patterns on the back side and aluminium patterns on the front side of SiC free-standing membranes, D) Optical images showing: i) Excellent optical transparency of GaN membranes by observing smart phone pixels through a GaN membrane (left), and without GaN membranes (right), ii) the good alignment of photoresist patterns on the back side and aluminium patterns on the front side of GaN free-standing membranes, E) Optical images showing good alignment of photoresist patterns on the back side and aluminium patterns on the front side of SiN free-standing membranes F) Complex SiC structures on soft polymer substrates: i) Optical image of a SiC/ Polyimide (PI) flower on a water droplet ii) SEM images of a SiC/PI spider web structure with an ant on it iii) Optical image of serpentine SiC structures on a PDMS sheet bending on a tube.

shown in the left panel of **Figure 3**A. We applied compressive forces to bend a 200 nm-thick SiC on 10 µm-thick PI film with a minimum bending radius of 3 mm over 1000 cycles. The strain in the SiC layer was approximately $\varepsilon \approx \frac{t}{2R} = 0.17\%$, which was below the fracture limit of the SiC thin film. To experimentally

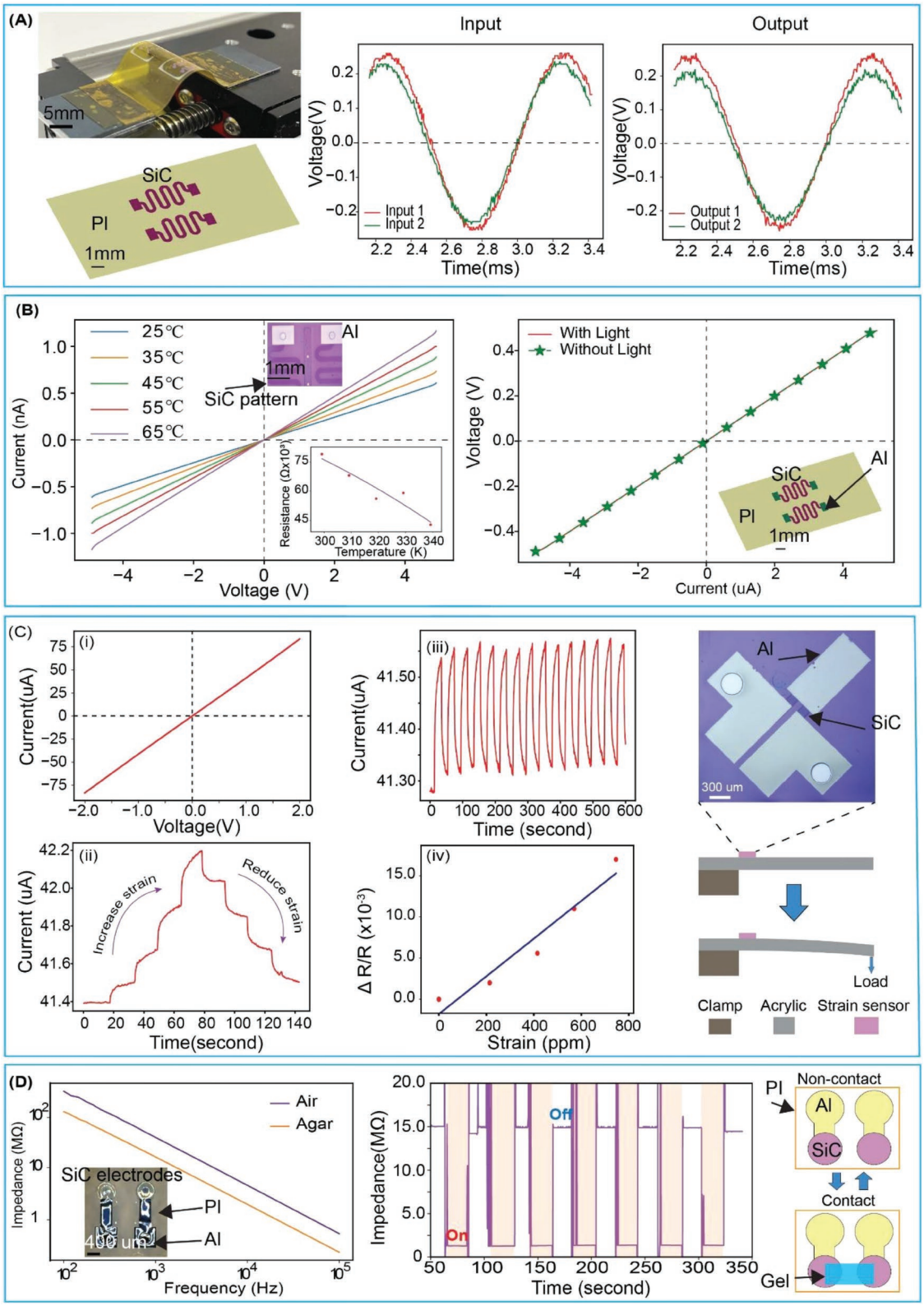

Figure 3. Demonstration of SiC/ PI electronics devices. A) Mechanical characterization set-up for the fatigue test of SiC electrodes on a PI substrate (left), the voltage characteristic comparison of the electrode before and after the bending test (right). B) *I–V* characteristic of a temperature sensor (left) and the effect of illumination on the *I–V* characteristic of that temperature sensor (right), inset shows the variation of resistance against temperatures. C) Demonstration of SiC strain sensor: i) The *I–V* characteristic of a strain sensor, ii) Repeatability test of a strain sensor, iii) Change in the current of the sensor under different loads, iv) The relationship between the resistance change and the induced strain. D) Impedance sensor: comparison of the impedance measured in a frequency range of 100 Hz to 100 kHz at contact and non-contact modes capacitance in agar gel and in the air (up), on-off measurement of the sensor (down).

verify this, we introduced an AC current into one terminal of SiC devices and measured the output current at the other terminal. A comparable value in the magnitude and frequency of the input and output signals suggested that the devices were free of cracks after the cyclic bending experiment (see the right panel of Figure 3A). The mechanical flexibility of our WBG system was attributed to reduced bending stiffness in a bilayer of SiC-on-polyimide compared to the original SiC-on-Si wafer. Specifically, due to the small thickness of the SiC film, the moment of inertia is mainly dominated by the polyimide layer, which can be expressed as:

$$M_{\mathrm{SiC/S}} = \frac{E_{\mathrm{SiC}}^2 t_{\mathrm{SiC}}^4 + E_{\mathrm{S}}^2 t_{\mathrm{S}}^4 + E_{\mathrm{SiC}} E_{\mathrm{S}} t_{\mathrm{SiC}} t_{\mathrm{S}} \left(2t_{\mathrm{SiC}}^2 + 3t_{\mathrm{SiC}} t_{\mathrm{S}} + 2t_{\mathrm{S}}^2\right)}{12\left(E_{\mathrm{SiC}} t_{\mathrm{SiC}} + E_{\mathrm{S}} t_{\mathrm{S}}\right)} \quad (1)$$

where $M_{\mathrm{SiC/S}}$ is the bending stiffness of the multilayer structures; E_{SiC} and t_{SiC} are the elastic modulus and thickness of the SiC layers respectively, and E_{S} and t_{S} are the elastic modulus and thickness of the substrate, respectively. Accordingly, the bending stiffness of 200-nm SiC on polyimide is ≈ 52 times lower than that of SiC-on-Si with a similar thickness, allowing for significantly enhanced deformation in flexible electronics applications. Further details on the mechanical flexibility of the device for this mechanical test can be found in Figures S6 and S7 (Supporting Information). This serpentine SiC architecture was utilized in temperature sensors, and light sensitivity test presented in the following sections.

For in vitro organ-on-chip and in vivo implant applications, measurement of temperature provides vital information such as the response of immune systems, monitoring of wound healing, and management of thermal therapy and thermal stimulation.[38] In particular, for in vitro systems that employ physiological monitoring combined with image-based analysis, temperature sensors insensitive to photo illumination are desirable to avoid signal crosstalk.[39] In this regard, our flexible WBG platform emerges as an excellent candidate thanks to its stable electrical properties to photons within the visible range. As presented in Figure 3B (right), we demonstrated an n-type SiC on polyimide temperature sensors with a measurement range of 25 to 65 °C. The sensors (with a carrier concentration of $\approx 10^{17}$ cm^3) exhibited an enhancement in conductivity with increasing temperature, which was attributed to an increase in charge carrier density (i.e., electrons for n-type 3C-SiC) generated by thermal activation. Specifically, raising the temperature from 25 to 65 °C resulted in an increase in the conducting current of 91.2%, corresponding to a temperature coefficient of resistance ($TCR = (\Delta R/R)/\Delta T$) of 11900 (ppm/K) where R is resistance at a reference temperature, ΔR is resistance change, and ΔT is temperature change. Using the Arrhenius approximation, the conductivity (σ) can be described as: $\sigma \propto \exp(-E_{\mathrm{A}}/k_{\mathrm{B}}\mathrm{T})$, where T is the temperature and k_{B} is the Boltzmann constant. The relationship between the change in conductivity versus temperature can be derived as: $-\ln\left(\frac{\sigma}{\sigma_0}\right) = E_{\mathrm{a}} \times (1/k_{\mathrm{B}}T - 1/k_{\mathrm{B}}T_0)$. From the slope of the fitted curve for these equations (Figure S4, Supporting Information), we estimated an activation energy of 120 meV at room temperature, resulting in the observed large TCR. Figure 3B (left) shows the current-voltage characteristics of SiC temperature sensors under dark and light conditions, indicating that the electrical property of our devices was unaffected by illumination. For low-doped Si counterparts, it is worth noting that a photoresponse-compensated circuitry is required for lab-on-chip systems that work under fluorescence microscopy.[39] The additional circuit makes the overall in vitro systems bulkier. Therefore, in many cases, it cannot completely remove the photoresponse from the read-out signal. The visible-light-blind sensors in our flexible system offer a novel solution for more reliable temperature monitoring applications, especially for lab-on-chip and organ-on-chip studies.

2.3.2. Strain Sensors for Mechanotransduction

The crystal structure of SiC can be deformed under mechanical stress, which may change its energy band structure. This phenomenon, namely the piezoresistive effect, can be applied to develop soft WBG material-based strain and pressure sensors for health monitoring applications. Specifically, as demonstrated in the abovementioned experiment, the conductivity of SiC is insensitive to photo illumination, which makes it an attractive material for underpinning on-chip mechanotransduction studies combined with optical observation. To demonstrate this concept, we developed an n-type SiC-on-polyimide strain sensor with a U-shape configuration as shown on the right panel of Figure 3C. Based on our previous studies on the theory of the strain effect on cubic SiC, we selected the (100) crystal orientation to maximize the strain sensitivity of n-type SiC sensors.[40] To quantify the strain induced into the sensing element (i.e., n-type SiC resistors), we embedded the released SiC-on-polyimide sensors onto an acrylic beam with a dimension of 10 mm × 100 mm × 1 mm for the width, length, and thickness, respectively. The ease of releasing soft SiC electronics from the original Si substrate obtained from our technique is the key to transferring this new platform to any arbitrary template. We then applied a bending test to the acrylic beam using known loads at its free-end and measured the induced strain using a reference metal strain gauge attached to a similar beam with the same dimension. Figure 3D(ii) shows the sensor response to applied strains varying from 0 to 800 ppm. Evidently, increasing the applied tensile strain leads to an increase in the output current of the sensors. A cyclic bending test with a constant strain of 500 ppm results in a repeatable output signal of ≈0.6% change in the current, Figure 3D(iii). From the resistance change and the applied strain in Figure 3D(iv), we estimate the gauge factor ($GF = \frac{\Delta R/R}{\varepsilon}$, where ε is the induced strain, and ΔR/R is the relative resistance change) of our flexible 3C-SiC to be –12.5. The magnitude of the gauge factor in n-type 3C-SiC is at least sixfold larger than that of metallic materials and exhibits opposite behavior (i.e., the conductivity is enhanced with tensile strain). This high sensitivity in n-type flexible SiC nanomembranes is attributed to the electron transfer phenomenon,[41] where the deformation of the conduction bands under tensile strain leads to the re-location of free electrons (see the Supporting Information). In particular, the first principal analysis model for n-type 3C-SiC nanosheet suggested that inducing a tensile strain in [100] orientation will move the longitudinal [100] energy valley upward and

shift the [010] and [001] transverse energy valleys downward.[42] As a result, free electrons in these valleys will repopulate following the Boltzmann distribution (i.e., electrons from the longitudinal direction will move to the lower energy levels in transverse directions). As the transverse mobility of electrons is higher than the longitudinal mobility, having more electrons in the transverse valleys results in an enhancement of the total mobility (or conductivity), which agrees with our experimental observations. There is a significant interest in the measurement of contraction forces in skeletal muscles to evaluate the efficiency of therapeutic procedures. Our soft SiC-on-polyimide, with excellent mechanical flexibility, optical transparency, high sensitivity, and optical stability offers a potentially powerful tool for elucidating relevant cues of muscular disorders.

2.3.3. Impedance Sensors for Contact and Physiology Measurement

Our recent study revealed the high feasibility of SiC nanomembranes for impedance sensors for real-time monitoring of radio frequency (RF) ablation procedures, owing to their zero-hydrolysis rate, negligible water penetration, and extremely low ion diffusivity.[28] However, the existing platform employs rigid SiC-on-glass templates, which limits their implementation in surgical endoscopes. Flexible SiC on transparent polymers such as PDMS or polyimide, on the other hand, can expand their current capability to soft surgical platforms or bioimplants, such as balloon catheters and deformable stents, by transferring our new devices onto the curvilinear surfaces of these medical tools. To demonstrate this concept, we developed transparent SiC-on-polyimide impedance sensors, where a pair of circular SiC electrodes was used to detect the physical contact between devices and biotissue (see Figure S7C, Supporting Information). Aluminum metal traces were implemented to connect the SiC sensors to an external readout circuit. For the sake of simplicity, we employed a hydrogel formed by mixing agarose powder with PBS solution as a phantom tissue model. Details of the preparation of phantom tissue are shown in Note S3 (Supporting Information). As illustrated in Figure 3D – inset, when the two SiC nanomembrane electrodes made a physical contact with the phantom tissue, the existing ions in the gel formed an additional conducting channel between the electrodes, leading to a decrease in the total impedance. The significant change in the impedance can be observed by sweeping the measurement frequency from 100 Hz to 0.1 MHz under the non-contact and contact states. We further demonstrate the repeatability of the SiC-on-polyimide sensors by measuring the impedance at a fixed frequency of 10 kHz, which detected the touching and non-touching modes for several cycles.

2.4. Bio-Application of Soft SiC-Based Devices

2.4.1. Biocompatibility for Bio-Implantable Applications

It is essential to validate the biocompatibility of the materials used. In this regard, the optical transparency of both the SiC sensing element and the polyimide substrate serves as an excellent tool for in vitro validation of these materials. Using the cell line MDA MB 231 as a test vehicle, we characterized the biocompatibility of our soft devices by counting the cell numbers and observing their morphology. As shown in Figure S3 (Supporting Information), the number of cells attached to the SiC/PI structure increased after 24, 48, and 120 h. The number of dead cells remained almost zero while the number of growth cells increased linearly, which indicates no cytotoxic effect. The cell counts on silicon carbide were comparable to that of the control sample after five days of growth, and the microscopic image shows that cells were well anchored onto the silicon carbide surface. As well as biocompatibility, we also investigated the long-term stability of SiC electrodes in biofluids. The SiC electrodes were soaked into PBS solution at a temperature of 70 °C. The electrical resistance of the SiC electrode was measured every 24 h for a total period of 192 h. The results show that the electrical resistance of the SiC electrode is stable under the soaking test (Figure S10, Supporting Information).

2.4.2. In Vitro Cell Monitoring Applications

Cell culturing and in vitro tissue engineering are crucial methods in the fields of cell biology and drug development, as they allow for fundamental investigation of intracellular activities and the efficacy of new medical treatments. Recent studies suggest the promise of integrated bioelectronics into to lab-on-chip and organ-on-chip systems that enable real time and continuous observation of biological behaviors without changing the culturing environment.[43,44] In this regard, SiC electronics with excellent biocompatibility and optical transparency validated in the above experiments represent exciting opportunity for remote cell culturing and monitoring applications. To demonstrate this feasibility, we utilized a long-lived and transparent SiC comb electrodes on flexible PI substrates was introduced as an impedance sensor to detect the proliferation of cancer cells. In this study, the LS513 cells, a colorectal carcinoma cell line derived from a patient diagnosed with a Dukes'C mucin-secreting cecal tumor, were used. The experimental setup for cell culturing is presented in Figure S9 (Supporting Information). The SiC comb electrodes possess characteristics that make them suitable for studying cell proliferation and differentiation, including their long lifespan and transparency, which allow for direct observation through microscopes.

Figure 4A (right) illustrates the sensing concept of SiC-based cell proliferation sensor, in which the proliferation of cells on the surface of the electrodes prevents the ions in the electrolyte from reaching the electrodes. This decrease in the number of ions on the top surface of the comb electrodes leads to an increase in the impedance of the sensor. The impedance was measured after 48 and 96 h from the start of cell culturing. The data reveals a notable increase in the impedance, as shown in Figure 4A (middle). Furthermore, real-time observation of cell proliferation from an optical microscope shows a consistent trend with that monitored by the SiC impedance sensor, Figure 4A (left). The use of SiC comb electrodes on flexible PI substrates for simultaneous impedance sensing and optical imaging provide a promising tool for remote cell biology and drug development that can potentially minimize labor cost and stabilize the cell growth environment.

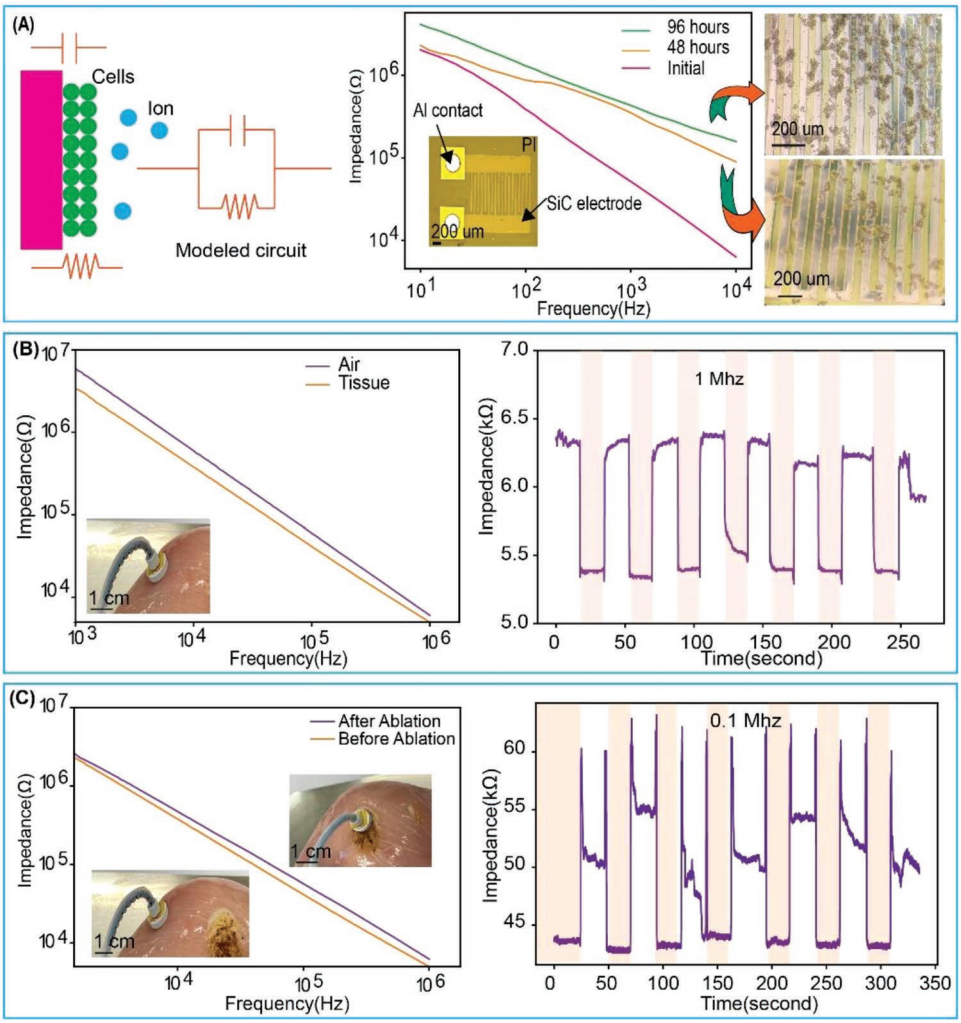

Figure 4. Biomedical application of SiC-based electronic devices. A) The cell proliferation test for cancer cells, and the see-through microscope images of cell proliferation. B) The detection of tissues as a potential to detect cancer tumors (left), and the on-off test showing the sensibility of detecting tissues (right). C) The capability of the sensor to recognize tissue before and after ablation (left), and the on-off test (right).

2.4.3. Soft Electronics for Multimodal Surgical Robotics

The ability to transfer chemically stable WBG materials onto flexible and transparent polymer can extend their capability to robotics applications where soft electronics and sensors offer powerful functionalities for on-site diagnostics and medical treatments. Soft surgical robots are an emerging technology that can assist with minimally invasive surgeries where traditional surgical tools are rigid and bulky that require a large incision. To improve their accuracy and effectiveness, these soft robots can be integrated with flexible sensors and cameras that help surgeons detect and observe tissues and organs inside the body. However, commercial rigid sensors possess several drawbacks that reduce the flexibility of the robot arms and pose malfunctioning due to mechanical mismatch with the soft body of robots. Therefore, flexible sensors are imperative to enable a seamless integration onto soft surgical robots. Here we demonstrate the capability of our new technology in producing a SiC impedance sensor that can realize different tissues with the potential for cancer treatment by thermal ablation. In particular, in case of poor illumination conditions, recognizing different tissues is challenging for surgeons; the impedance sensor, therefore, provides an alternative to detect tumor cells when the robot tips contact with tissues. The sensors are made of two circular SiC electrodes with parallel Al contact supported by a 7 μm PI flexible substrate that makes them highly bendable. The sensor was then detached from the Si substrate and mounted onto the end-effector of a soft robot actuated by Soft Microtubue Artificial Muscle (SMAM). The detail of the configuration of SMAM robots can be found in our previous studies.[45] We demonstrated the functionalities of our sensors and SMAM robot on chicken tissue, Figure 4B. The sensors show a significant change in the impedance when the end-effector touches the tissue, (Figure 4B,C). We then applied radio frequency (RF) thermal ablation to remove targeted tissue, which led to a modification of the treated areas that is visually observable. Using the integrated SiC sensors, we can differentiate the ablated tissues from the non-treated ones, that show an increase in the impedance after the RF ablation, Figure 4C. This increasing is resulted from the dehydration and

carbonization of ablated tissues, which were reported in previous literatures.[46,47] Furthermore, the transparency of the SiC electrode offers the capability of real-time observation through the robotic end effector (Figure S11, Supporting Information). Our demonstration indicates the possibility to develop an all-in-one surgical robot capable of biological sensing and medical therapy, where flexible, transparent electronics can be well incorporated into soft actuation systems.

2.5. 3D Origami/ Kirigami-Inspired SiC/ PI base Structures

Most existing flexible WBG electronics are built on planar platforms, which offer mechanical bendability but limited stretchability. In addition, previous studies indicated promising applications of compliant, 3D structures in fields ranging from microrobots,[48,49] to optics,[50] drug delivery study,[43] unusual electronics,[51] and tissue engineering,[52] which are not possible with standard 2D systems. One of the main burdens that hinder the development of 3D architectures for WBG devices is the sacrificial layer for releasing the planar precursors. Additional steps requiring the removal of this sacrificial layer, which through the use of hazardous chemical etching (e.g., removing an Al sacrificial layer in SiC or ZnO layer from GaN) make conventional transfer printing process not suitable for subsequent buckling steps.

Compared to conventional methods, our novel engineering approach allows for the utilization of a mechanical buckling strategy to transform 2D precursors of WBG on polymer substrates to 3D buckling mesoscale structures. Lithography and dry etching on the backside enable the formation of functional elements (i.e., SiC), and standard microfabrication processes on the front side add and pattern other soft materials (e.g., metal interconnects, polyimide microstructures, and Ti/SiO_2 bonding sites), which facilitates bonding of the released 2D precursor to a pre-strained PDMS substrate. Following the release of the 2D precursor from Si, we temporarily attached this 2D precursor to a PDMS sheet before transferring it to a water-soluble tape. Ti/SiO_2 pads on the 2D precursor were then bonded to a pre-strained PDMS film using surface treatment with oxygen plasma. Removal of the water-soluble tape in warm water and releasing the pre-strain in the PDMS film caused the 2D, flexible SiC electronics to buckle into a 3D system.

We demonstrated a variety of 3D SiC mesostructures that can be used in a broad range of applications. The formation of these structures was in good agreement with the finite elemental analysis (FEA) results. For instance, a polyimide ribbon containing a SiC serpentine pattern can buckle into an arc shape under uniaxial buckling. The maximum strain induced into the SiC membranes was comparable to the mechanical yield strength of the SiC material, **Figure 5**A. Figure 5A–F shows the maximum principal strain distribution (positive for tensile strains and negative for compressive strains). Mechanical test results from previous research indicate an ultimate tensile strain of ≈0.29% and an ultimate compressive strain of 1.4% for thin-film silicon carbide.[53,54] Almost all SiC thin films remain within these fracture limits, with the exception of small, localized regions (Figure S14, Supporting Information). The strain levels in the SiC layer can be further reduced by introducing a kirigami-inspired design to the polyimide shape.[55] While SiC materials have been demonstrated for long-lived bioelectronics due to their chemical inertness, 3D configurations such as the as-fabricated serpentine structures could offer extra mechanical stretchability, allowing for the implanted WBG devices to adapt to tissue expansion and shrinking in long-term implants. Besides uniaxial strains, biaxial strains can also be applied to form more complex mesostructures such as table-like shapes and pyramid shapes. The formation of the table-like shape (Figure 5C) combined with the piezoresistive effect in SiC can be used for multi-modal pressure sensing applications, which were successfully demonstrated in Si materials.[56] Here, SiC as the sensing element in a 3D configuration can eliminate the need for optical compensation circuits. The pyramid shapes could be utilized in tissue-on-chip models, where biosystems such as organoids or myotubes are transferred into these 3D frameworks, establishing a 3D bioelectronic interface for long-term in vitro studies.[26] It is noteworthy to mention that the maximum strain in the table-like configuration was relatively large. However, this strain can be reduced by adding another encapsulation layer on top of the SiC layer to bring it closer to the neutral axis. The chemical inertness and transparency of constituent materials (SiC, polyimide, and PDMS) would enable real-time observation of biosystems using an inverted microscope, allowing simultaneous electrical physiological measurement with traditional image-based characterization approaches. Engineering the pre-strains induced into the PDMS film can create different 3D configurations (e.g., asymmetry) from the same 2D precursor, Figure 5E,F.

3. Conclusion

The present work introduces a new engineering route for the development of flexible wide bandgap materials by applying lithographic processes on both sides of free-standing nanomembranes taking advantage of their optical transparency and mechanical robustness. This approach allows for the stacking and patterning all structural and functional elements of soft electronics on a standard Si substrate, eliminating the requirement for the time-consuming transfer-printing step. This facile fabrication technique also facilitates the transformation of 2D precursors of wide bandgap semiconductors into complex 3D mesostructures through mechanical buckling. The diverse 2D and 3D architectures of wide bandgap materials combined with their multi-functionalities such as mechanical, thermal, and impedance sensing open exciting opportunities for organ-on-chip and stretchable implantable device applications.

4. Experimental Section

SiC Film Deposition: The Si substrates were cleaned using the RCA (Radio Corporation of America) process before depositing SiC on both sides. 200 nm SiC films were epitaxially grown on Si substrates using a hot wall chamber at 1250 °C. After carbonization of the SiC surface, SiH_4 and C_2H_6 were alternatively supplied for the epitaxy growth. An in situ doping method was then used to form n-type SIC using NH_3 as the dopant.

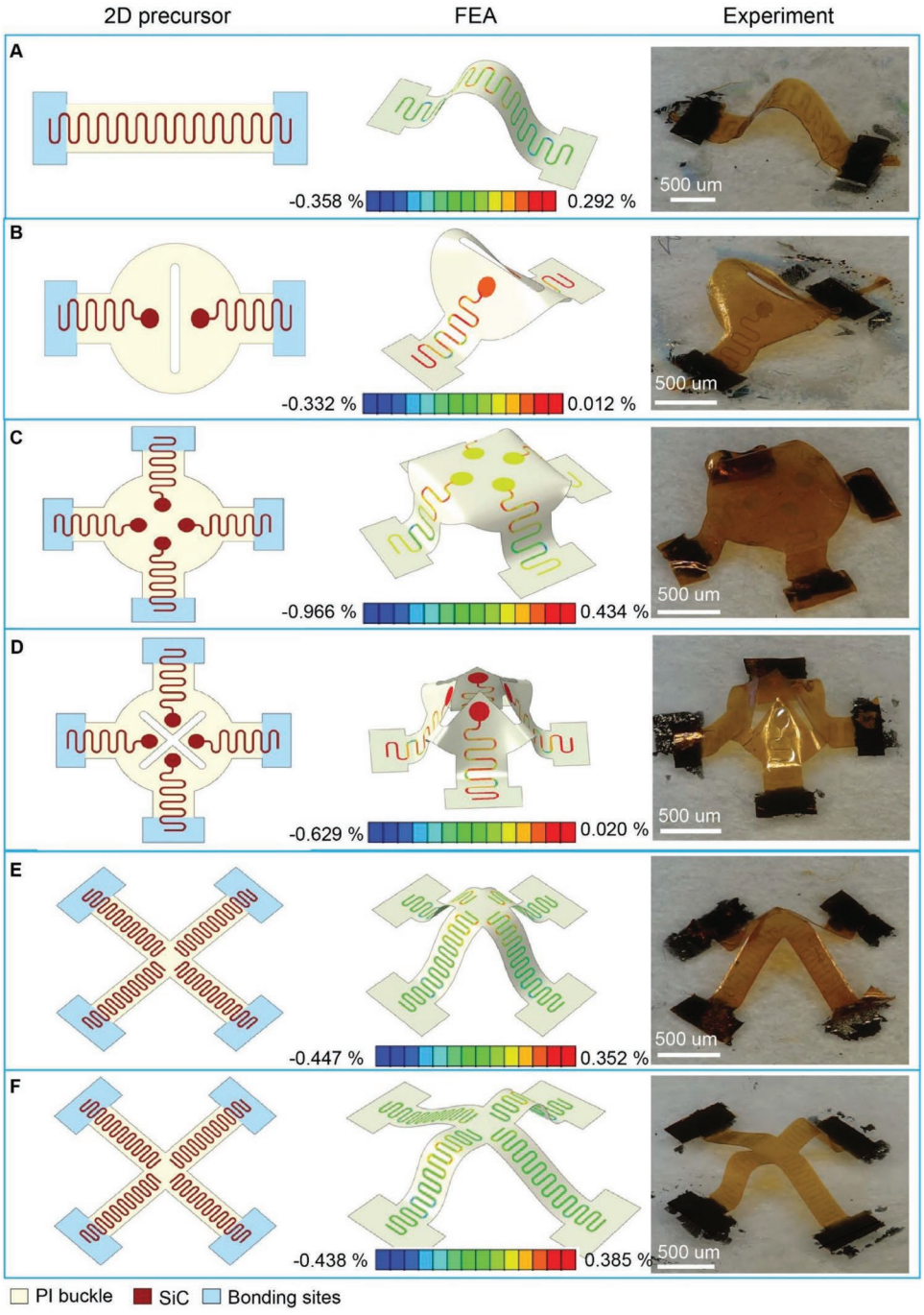

Figure 5. 3D SiC/ PI origami and kirigami-inspired mesostructures, from left to right are 2D

Figure 5. 3D SiC/ PI origami and kirigami-inspired mesostructures, from left to right are 2D precursors, FEA of 3D structures with strain distributions in the SiC layer, and optical images of 3D structures from experiments: A,B) uniaxial buckling structures using 50% pre-stretched PDMS. B–E) Biaxial buckling structures using 50% pre-stretched PDMS. F) unequal pre-stretch amount of PDMS on each side (20% and 8%).

Fabrication of Free-Standing SiC Membranes: The AZ5214 photoresist was patterned on the backside of SiC/Si/SiC wafers using the standard lithography process to form the opening pattern for SiC free-standing membranes. The backside SiC layer was then etched using inductively coupled plasma etching (SF_6 + O_2, for 2 min) until the SiC layer was exposed. KOH (30%) was used to etch the exposed Si at 80 °C for 10 h, leaving the square opening of the SiC layers on the other side. The wafer with SiC window was then cleaned using RCA to remove contamination.

Fabrication of SiC Mesostructures on Polyimide (PI) Flexible Substrate: Fabrication of SiC-based devices, including strain sensors, impedance sensors, and cell culture test devices, started with spin-coating (4000 rpm for 60 s), soft baking (110 °C for 60 s), and developing a layer of photoresist AZ5214 on the back side of SiC membranes. Next, a layer of aluminum (Al, 300 nm) deposited and patterned on the front sides of the SiC membrane served as contact electrodes. Subsequently, a layer of polyimide (PI, 7 µm) was spin-coated (3000 rpm for 60 s) and developed

(MIF 716 developer for 40 s) to serve as a flexible substrate. The back side of SiC was then dry etched using reactive ion etching (CHF_3+CH_4+O_2) for 11.5 min, leaving the SiC structures with Al electrodes on flexible substrates (PI). Details of the fabrication process are described in the Supporting Information.

Fabrication of 3D Origami and Kirigami-Inspired SiC/ PI-Based Structures: The fabrication of 3D origami/kirigami-inspired structures utilized compressive buckling approaches described in previous studies.[43,50] 2D precursors were fabricated using the same process described in the previous section. The membranes were bonded onto sticky PDMS substrates (2-mm thickness, ratio 45:1) to keep the 2D precursors flat after dry etching. After being transferred to water-soluble tapes (polyvinyl alcohol, PVA), 2D precursors were covered by shadow masks, leaving only bonding site patterns exposed. The bonding sites were formed by depositing a thin layer of Ti/ SiO_2 (50 nm/50 nm in thickness). Thin sheets of PDMS (0.5 mm in thickness, ratio 10:1) were casted and pre-stretched (50% biaxial strain) using customized stretch systems as platforms for the buckling processes. The 2D precursors/PVA tape and PDMS platforms were then treated with oxygen plasma to create the surface-to-surface hydroxyl groups for the bonding. The 2D precursors/ PVA tapes were then laminated onto the surfaces of the pre-stretched PDMS, followed by heating at 70 °C for 4 min to enhance the bonding strength. After removing PVA tape using water, releasing the pre-strain PDMS lead to the transformation of 2D precursors to 3D origami/kirigami-inspired structures. The fabrication process is described in the Supporting Information.

Fabrication of 2D SiC on PDMS Substrates: After patterning the photoresist AZ5214 on the back side of SiC membranes, there were two methods to transfer SiC structures onto PDMS substrates. The first method was dry etching the bilayer SiC/ PDMS using RIE after spin-coating PDMS on the front side of the membranes (4000 rpm for 60 min to form 25 µm thickness). The second method used Van der Waal forces between SiC and PDMS to generate the bonding between these two layers. Having the photoresist patterned, the membranes were transferred to PDMS substrates (0.5 mm in thickness) so that the front side of the membranes contacted the surfaces of the PDMS sheets. Dry etching and delaminating the Si frames left the SiC patterns sticking onto the PDMS.

FEA of 3D Buckling Process: All the simulations in this paper used commercial FEA software (ABAQUS) to predict the transformation of 2D precursors into 3D buckling shapes. FEA used 4-node shell elements (S4R) for the PI and SiC layers. Mesh convergent analysis was conducted to guarantee the accuracy of the simulation and optimize the element size to save computational time. Linear elastic material models were assigned for PI and SiC due to the small strain. The Young's modulus (E) and Poisson's ratio (υ) were E_{PI} = 2.5 GPa and υ_{PI} = 0.34 for PI; E_{SiC} = 330 GPa, υ_{SiC} = 0.28 for SiC. The results from linear perturbation analysis served as the initial geometric imperfection for the post-buckling simulation.

Stretchability Test: One end of the SiC serpentine structure/ PI bilayers was fixed, and the other end was connected to a movable station controlled using a linear motor. The motion of the movable station was used to apply compressive strain. An oscilloscope (Tektronic, DPO7104) was used to characterize the performance of the devices before and after 1000 cycles of bending. The Agarose gel was employed as contact with the SiC electrode.

Electrical Measurement: The current–voltage characteristics were obtained using a semiconductor device parameter analyzer (Agilent B1500). Temperature sensing was conducted using a controlled thermal chuck (±0.1 °C), while the actual temperature on the devices was measured through a reference sample with the same geometrical conditions.

The impedance measurement was conducted using an LCR meter (i.e., HP 4284A). To measure the impedance, the LCR scanned an AC frequency from 100 Hz to 0.1 MHz. Agarose gel powder was used to produce a phantom tissue for the test. The process to make this phantom tissue is provided in the Supporting Information.

To conduct the strain sensor measurement, the strain sensor which comprises SiC/Al/ PI was bonded on an acrylic plate. One end of the acrylic plate was fixed, while the free end contacted the load. In this paper, a weight of 20 g each was supplied at 20 s intervals. Then, to unload the free end, the weights were sequentially removed one by one at an interval of 20 s.

Cell Culture Test: The MDA MB 231 cells were obtained from ATCC and were cultured in T75 flasks at 37 °C in a humidified atmosphere with 5% CO_2. The cells were grown and maintained in DMEM/F12 (Gibco, Thermo Fisher Scientific, Waltham, MA, USA) medium with 10% fetal bovine serum (FBS) and 1% penicillin/Streptomycin. The cells were harvested at 80% confluency for seeding on the test material. Before seeding the cells on the test material for the biocompatibility assay, silicon carbide membranes were sterilized with 80% ethanol and washed three times with sterile 1× Hank's balanced salt solution (HBSS) followed by UV radiation for 30 mins. After that, the cells were directly seeded on the sterile material and cultured for subsequent time points. The cells were further analyzed for cell morphology and cell proliferation.

The cells were imaged in brightfield mode using a Nikon Eclipse Ti2 microscope. For cell proliferation, a cell counting kit (WST-8 from abcam) dye was added to the test material and incubated at 37 °C. The cells were counted by the colorimetric method.

Cancer Cell Proliferation Culture and Observation: The LS513 cells were obtained from ATCC and were cultured in T75 flasks at 37 °C in a humidified atmosphere with 5% CO_2. The cells were grown and maintained in DMEM/F12 (Gibco, Thermo Fisher Scientific, Waltham, MA, USA) medium with 10% fetal bovine serum (FBS) and 1% penicillin/Streptomycin. The cells were harvested at 80% confluency for seeding on the test material. Before seeding the cells on the test material for the biocompatibility assay, silicon carbide membranes were sterilized with 80% ethanol and washed three times with sterile 1× Hank's balanced salt solution (HBSS) followed by UV radiation for 30 min. After that, the cells were directly seeded on the sterile material and cultured for subsequent time points. The cells' growth and morphology were analysed on the device. The cells proliferate into identical healthy specimens, and the number of cells increases exponentially. The comb electrodes were imaged, and the impedance was measured every 48 h. The cells were imaged in brightfield mode using a Nikon Eclipse Ti2 microscope. The impedance was measured using a CHI-660E EIS workstation. The set-up for the cell proliferation test is shown in Figure S8 (Supporting Information).

The Fabrication of a Flexible Surgical Robot: The flexible robotic arm was composed of a bending segment and a flexible body that allowed for versatile movements. The bending motion was achieved through the use of triangular cut-outs in a PTFE tube, which were carefully crafted with a sharp knife to create an asymmetrical design. The remaining tube served as the bending segment and was actuated by a Soft Microtubue Artificial Muscle (SMAM), a fluid-driven device that had been successfully developed and tested. To operate the SMAM, it was elongated to 50% of its original length via a hydraulic transmission tube that was concealed within the flexible body. By adjusting the pressure within the SMAM, the device could generate different levels of pulling force, allowing for greater control over the bending motion. The proximal end of the muscle was securely attached to a 3D printed base, while the distal end was connected to the end of the cut-out PTFE tube. In terms of functionality, the robotic arm could achieve two-way bending motions with a single actuator source. When the hydraulic pressure within the SMAM decreased, it became shorter, causing the cutout tube to bend toward one side. Conversely, when the pressure increased, the SMAM became longer than its original length, causing the tube to bend toward the opposite side.

Supporting Information

Supporting Information is available from the Wiley Online Library or from the author.

Acknowledgements

This work was partially funded by the Australian Research Council (DE200100238, and DP230101312) and was performed in part at the Queensland node of the Australian National Fabrication Facility, a company established under the National Collaborative Research Infrastructure Strategy to provide nano- and microfabrication facilities for Australia's researchers. The authors acknowledge the facilities, and the scientific and technical assistance, of the Microscopy Australia Facility at the Centre for Microscopy and Microanalysis (CMM), The University of Queensland. The authors would like to thank Dang Vu Nhat Linh for his assistance in the mechanical tests in this work.

Open access publishing facilitated by University of New South Wales, as part of the Wiley - University of New South Wales agreement via the Council of Australian University Librarians.

Conflict of Interest

The authors declare no conflict of interest.

Data Availability Statement

The data that support the findings of this study are available from the corresponding author upon reasonable request.

Keywords

3D microstructures, origami/kirigami-inspired microstructures, stretchable microarchitectures, wide bandgap materials

Received: October 11, 2022
Revised: March 24, 2023
Published online:

[1] X. Cheng, Y. Zhang, *Adv. Mater.* **2019**, *31*, 1901895.
[2] D. H. Kim, N. Lu, R. Ma, Y. S. Kim, R. H. Kim, S. Wang, J. Wu, S. M. Won, H. Tao, A. Islam, K. J. Yu, T. Il Kim, R. Chowdhury, M. Ying, L. Xu, M. Li, H. J. Chung, H. Keum, M. McCormick, P. Liu, Y. W. Zhang, F. G. Omenetto, Y. Huang, T. Coleman, J. A. Rogers, *Science* **2011**, *333*, 838.
[3] Y. Liu, M. Pharr, G. A. Salvatore, *ACS Nano* **2017**, *11*, 9614.
[4] J. A. Rogers, T. Someya, Y. Huang, *Science* **2010**, *327*, 1603.
[5] S. Mousavi, M. T. Thai, M. Amjadi, D. Howard, S. Peng, T. N. Do, C. H. Wang, *J. Mater. Chem. A* **2022**, *10*, 13673.
[6] S. Peng, S. Wu, Y. Yu, Z. Sha, G. Li, T. T. Hoang, M. T. Thai, T. N. Do, D. Chu, C. H. Wang, *J. Mater. Chem. A* **2021**, *9*, 26788.
[7] S. Han, J. Kim, S. M. Won, Y. Ma, D. Kang, Z. Xie, K. T. Lee, H. U. Chung, A. Banks, S. Min, S. Y. Heo, C. R. Davies, J. W. Lee, C. H. Lee, B. H. Kim, K. Li, Y. Zhou, C. Wei, X. Feng, Y. Huang, J. A. Rogers, *Sci. Transl. Med.* **2018**, *10*, aan4950.
[8] K. H. Lee, X. Ni, J. Y. Lee, H. Arafa, D. J. Pe, S. Xu, R. Avila, M. Irie, J. H. Lee, R. L. Easterlin, D. H. Kim, H. U. Chung, O. O. Olabisi, S. Getaneh, E. Chung, M. Hill, J. Bell, H. Jang, C. Liu, J. Bin Park, J. Kim, S. B. Kim, S. Mehta, M. Pharr, A. Tzavelis, J. T. Reeder, I. Huang, Y. Deng, Z. Xie, C. R. Davies, et al., *Nat Biomed Eng* **2019**, *4*, 148.
[9] L. Tian, Y. Li, R. C. Webb, S. Krishnan, Z. Bian, J. Song, X. Ning, K. Crawford, J. Kurniawan, A. Bonifas, J. Ma, Y. Liu, X. Xie, J. Chen, Y. Liu, Z. Shi, T. Wu, R. Ning, D. Li, S. Sinha, D. G. Cahill, Y. Huang, J. A. Rogers, *Adv. Funct. Mater.* **2017**, *27*, 1701282.
[10] S. R. Madhvapathy, Y. Ma, M. Patel, S. Krishnan, C. Wei, Y. Li, S. Xu, X. Feng, Y. Huang, J. A. Rogers, *Adv. Funct. Mater.* **2018**, *28*, 1802083.
[11] L. Tian, B. Zimmerman, A. Akhtar, K. J. Yu, M. Moore, J. Wu, R. J. Larsen, J. W. Lee, J. Li, Y. Liu, B. Metzger, S. Qu, X. Guo, K. E. Mathewson, J. A. Fan, J. Cornman, M. Fatina, Z. Xie, Y. Ma, J. Zhang, Y. Zhang, F. Dolcos, M. Fabiani, G. Gratton, T. Bretl, L. J. Hargrove, P. V. Braun, Y. Huang, J. A. Rogers, *Nat Biomed Eng* **2019**, *3*, 194.
[12] A. Koh, D. Kang, Y. Xue, S. Lee, R. M. Pielak, J. Kim, T. Hwang, S. Min, A. Banks, P. Bastien, M. C. Manco, L. Wang, K. R. Ammann, K. I. Jang, P. Won, S. Han, R. Ghaffari, U. Paik, M. J. Slepian, G. Balooch, Y. Huang, J. A. Rogers, *Sci. Transl. Med.* **2016**, *8*, aaf2593.
[13] Y. Song, J. Min, Y. Yu, H. Wang, Y. Yang, H. Zhang, W. Gao, *Sci. Adv.* **2020**, *6*, 9842.
[14] N. P. Tipnis, D. J. Burgess, *Int. J. Pharm.* **2018**, *544*, 455.
[15] A. H. Park, S. H. Lee, C. Lee, J. Kim, H. E. Lee, S. B. Paik, K. J. Lee, D. Kim, *ACS Nano* **2016**, *10*, 2791.
[16] G. Shin, A. M. Gomez, R. Al-Hasani, Y. R. Jeong, J. Kim, Z. Xie, A. Banks, S. M. Lee, S. Y. Han, C. J. Yoo, J. L. Lee, S. H. Lee, J. Kurniawan, J. Tureb, Z. Guo, J. Yoon, S. Il Park, S. Y. Bang, Y. Nam, M. C. Walicki, V. K. Samineni, A. D. Mickle, K. Lee, S. Y. Heo, J. G. McCall, T. Pan, L. Wang, X. Feng, T. il Kim, et al., *Neuron* **2017**, *93*, 509.
[17] P. Gutruf, R. T. Yin, K. B. Lee, J. Ausra, J. A. Brennan, Y. Qiao, Z. Xie, R. Peralta, O. Talarico, A. Murillo, S. W. Chen, J. P. Leshock, C. R. Haney, E. A. Waters, C. Zhang, H. Luan, Y. Huang, G. Trachiotis, I. R. Efimov, J. A. Rogers, *Nat. Commun.* **2019**, *10*, 5742.
[18] V. K. Samineni, J. Yoon, K. E. Crawford, Y. R. Jeong, K. C. McKenzie, G. Shin, Z. Xie, S. S. Sundaram, Y. Li, M. Y. Yang, J. Kim, D. Wu, Y. Xue, X. Feng, Y. Huang, A. D. Mickle, A. Banks, J. S. Ha, J. P. Golden, J. A. Rogers, R. W. Gereau, *Pain* **2017**, *158*, 2108.
[19] P. Gutruf, V. Krishnamurthi, A. Vázquez-Guardado, Z. Xie, A. Banks, C. J. Su, Y. Xu, C. R. Haney, E. A. Waters, I. Kandela, S. R. Krishnan, T. Ray, J. P. Leshock, Y. Huang, D. Chanda, J. A. Rogers, *Nat. Electron.* **2018**, *1*, 652.
[20] P. Gutruf, J. A. Rogers, *Curr. Opin. Neurobiol.* **2018**, *50*, 42.
[21] J. Ausra, M. Wu, X. Zhang, A. Vázquez-Guardado, P. Skelton, R. Peralta, R. Avila, T. Murickan, C. R. Haney, Y. Huang, J. A. Rogers, Y. Kozorovitskiy, P. Gutruf, *Proc. Natl. Acad. Sci. USA* **2021**, *118*, 2025775118.
[22] J. T. Reeder, Z. Xie, Q. Yang, M.-H. Seo, Y. Yan, Y. Deng, K. R. Jinkins, S. R. Krishnan, C. Liu, S. McKay, E. Patnaude, A. Johnson, Z. Zhao, M. J. Kim, Y. Xu, I. Huang, R. Avila, C. Felicelli, E. Ray, X. Guo, W. Z. Ray, Y. Huang, M. R. MacEwan, J. A. Rogers, *Science* **2022**, *377*, 109.
[23] T.-K. Nguyen, M. Barton, A. Ashok, T.-A. Truong, S. Yadav, M. Leitch, T.-V. Nguyen, N. Kashaninejad, T. Dinh, L. Hold, Y. Yamauchi, N.-T. Nguyen, H.-P. Phan, *Proc Natl Acad Sci U S A* **2022**, *119*, 2203287119.
[24] Y. S. Choi, R. T. Yin, A. Pfenniger, J. Koo, R. Avila, K. Benjamin Lee, S. W. Chen, G. Lee, G. Li, Y. Qiao, A. Murillo-Berlioz, A. Kiss, S. Han, S. M. Lee, C. Li, Z. Xie, Y. Y. Chen, A. Burrell, B. Geist, H. Jeong, J. Kim, H. J. Yoon, A. Banks, S. K. Kang, Z. J. Zhang, C. R. Haney, A. V. Sahakian, D. Johnson, T. Efimova, Y. Huang, et al., *Nat. Biotechnol.* **2021**, *39*, 1228.
[25] Y. Park, C. K. Franz, H. Ryu, H. Luan, K. Y. Cotton, J. U. Kim, T. S. Chung, S. Zhao, A. Vazquez-Guardado, D. S. Yang, K. Li, R. Avila, J. K. Phillips, M. J. Quezada, H. Jang, S. S. Kwak, S. M. Won, K. Kwon, H. Jeong, A. J. Bandodkar, M. Han, H. Zhao, G. R. Osher, H. Wang, K. H. Lee, Y. Zhang, Y. Huang, J. D. Finan, J. A. Rogers, *Sci. Adv.* **2021**, *7*, 9153.
[26] H. Zhao, Y. Kim, H. Wang, X. Ning, C. Xu, J. Suh, M. Han, G. J. Pagan-Diaz, W. Lu, H. Li, W. Bai, O. Aydin, Y. Park, J. Wang,

Y. Yao, Y. He, M. T. A. Saif, Y. Huang, R. Bashir, J. A. Rogers, *Proc. Natl. Acad. Sci. USA* **2021**, *118*, 2100077118.
[27] X. Dai, W. Zhou, T. Gao, J. Liu, C. M. Lieber, *Nat. Nanotechnol.* **2016**, *11*, 776.
[28] T. K. Nguyen, S. Yadav, T. A. Truong, M. Han, M. Barton, M. Leitch, P. Guzman, T. Dinh, A. Ashok, H. Vu, V. Dau, D. Haasmann, L. Chen, Y. Park, T. N. Do, Y. Yamauchi, J. A. Rogers, N. T. Nguyen, H. P. Phan, *ACS Nano* **2022**, *16*, 10890.
[29] X. Chen, J. Dong, C. He, L. He, Z. Chen, S. Li, K. Zhang, X. Wang, Z. L. Wang, *Nano-Micro Lett.* **2021**, *13*, 67.
[30] D. J. Rogers, F. Hosseini Teherani, A. Ougazzaden, S. Gautier, L. Divay, A. Lusson, O. Durand, F. Wyczisk, G. Garry, T. Monteiro, M. R. Correira, M. Peres, A. Neves, D. McGrouther, J. N. Chapman, M. Razeghi, *Appl. Phys. Lett.* **2007**, *91*, 071120.
[31] S. K. Oh, M. U. Cho, J. Dallas, T. Jang, D. G. Lee, S. Pouladi, J. Chen, W. Wang, S. Shervin, H. Kim, S. Shin, S. Choi, J. S. Kwak, J. H. Ryou, *Appl. Phys. Lett.* **2017**, *111*, 133502.
[32] T. Pham, T. Nguyen, T. Dinh, S. Yadav, N. Nguyen, H. Phan, R. K. Vadivelu, A. Qamar, T.-A. Pham, T.-K. Nguyen, R. Kumar Vadivelu, T. Dinh, A. Qamar, S. Yadav, Y. Yamauchi, J. A. Rogers, N.-T. Nguyen, H.-P. Phan, Y. Yamauchi, S. Lucia Brisbane, A. Y. Yamauchi, J. A. Rogers, *Adv. Funct. Mater.* **2020**, *30*, 2004655.
[33] J. A. Fan, W. H. Yeo, Y. Su, Y. Hattori, W. Lee, S. Y. Jung, Y. Zhang, Z. Liu, H. Cheng, L. Falgout, M. Bajema, T. Coleman, D. Gregoire, R. J. Larsen, Y. Huang, J. A. Rogers, *Nat Commun* **2014**, *5*, 3266.
[34] K.-M. Chang, J.-Y. Chu, C.-C. Cheng, *IEEE Photonics Technol. Lett.* **2004**, *16*, 1807.
[35] X. Tan, Y. Lv, X. Zhou, X. Song, Y. Wang, G. Gu, H. Guo, S. Liang, Z. Feng, S. Cai, *Microelectron. Eng.* **2020**, *219*, 111143.
[36] H. Q. Nguyen, T. Nguyen, P. Tanner, T. K. Nguyen, A. R. M. Foisal, J. Fastier-Wooller, T. H. Nguyen, H. P. Phan, N. T. Nguyen, D. V. Dao, *Appl. Phys. Lett.* **2021**, *118*, 242104.
[37] S. J. Pearton, B. S. Kang, S. Kim, F. Ren, B. P. Gila, C. R. Abernathy, J. Lin, S. N. G. Chu, *J Phys Condens Matter* **2004**, *16*, R961.
[38] D. Lu, Y. Yan, R. Avila, I. Kandela, I. Stepien, M. H. Seo, W. Bai, Q. Yang, C. Li, C. R. Haney, E. A. Waters, M. R. MacEwan, Y. Huang, W. Z. Ray, J. A. Rogers, *Adv. Healthcare Mater.* **2020**, *9*, 2000942.
[39] U. G. Jung, K. Kuwana, Y. Ajiki, H. Takahashi, T. Kan, Y. Takei, K. Noda, E. Iwase, K. Matsumoto, I. Shimoyama, *J. Micromech. Microeng.* **2013**, *23*, 045015.
[40] H.-P. Phan, *Piezoresistive effect of p-type single crystalline 3C-SiC*, Springer International Publishing, **2017**.
[41] H. P. Phan, T. K. Nguyen, T. Dinh, H. H. Cheng, F. Mu, A. Iacopi, L. Hold, D. V. Dao, T. Suga, D. G. Senesky, N. T. Nguyen, *Phys. Status Solidi* **2018**, *215*, 1800288.
[42] K. Nakamura, T. Toriyama, S. Sugiyama, *Jpn. J. Appl. Phys.* **2011**, *50*, 06GE05.
[43] X. Wang, R. Feiner, H. Luan, Q. Zhang, S. Zhao, Y. Zhang, M. Han, Y. Li, R. Sun, H. Wang, T. L. Liu, X. Guo, H. Oved, N. Noor, A. Shapira, Y. Zhang, Y. Huang, T. Dvir, J. A. Rogers, *Extreme Mech. Lett.* **2020**, *35*, 100634.
[44] H. Zhao, Y. Kim, H. Wang, X. Ning, C. Xu, J. Suh, M. Han, G. J. Pagan-Diaz, W. Lu, H. Li, W. Bai, O. Aydin, Y. Park, J. Wang, Y. Yao, Y. He, M. T. A. Saif, Y. Huang, R. Bashir, J. A. Rogers, *Proc. Natl. Acad. Sci. USA* **2021**, *118*, 2100077118.
[45] M. T. Thai, P. T. Phan, T. T. Hoang, S. Wong, N. H. Lovell, T. N. Do, *Adv. Intell. Syst.* **2020**, *2*, 1900138.
[46] H. Lee, Y. Lee, C. Song, H. R. Cho, R. Ghaffari, T. K. Choi, K. H. Kim, Y. B. Lee, D. Ling, H. Lee, S. J. Yu, S. H. Choi, T. Hyeon, D. H. Kim, *Nat. Commun.* **2015**, *6*, 10059.
[47] T.-K. Nguyen, S. Yadav, T.-A. Truong, M. Han, M. Barton, M. Leitch, P. Guzman, T. Dinh, A. Ashok, H. Vu, V. Dau, D. Haasmann, L. Chen, Y. Park, T. N. Do, Y. Yamauchi, J. A. Rogers, N.-T. Nguyen, H.-P. Phan, *ACS Nano* **2022**, *16*, 10890.
[48] J. Kyu Park, K. Nan, H. Luan, N. Zheng, S. Zhao, H. Zhang, X. Cheng, H. Wang, K. Li, T. Xie, Y. Huang, Y. Zhang, S. Kim, J. A. Rogers, J. K. Park, K. Nan, S. Kim, H. Luan, Y. Huang, N. Zheng, T. Xie, S. Zhao, H. Wang, K. Li, H. Zhang, X. Cheng, Y. Zhang, J. A. Rogers, *Adv. Mater.* **2019**, *31*, 1905715.
[49] K. Malachowski, M. Jamal, Q. Jin, B. Polat, C. J. Morris, D. H. Gracias, *Nano Lett.* **2014**, *14*, 4164.
[50] H. Zhao, K. Li, M. Han, F. Zhu, A. Vázquez-Guardado, P. Guo, Z. Xie, Y. Park, L. Chen, X. Wang, H. Luan, Y. Yang, H. Wang, C. Liang, Y. Xue, R. D. Schaller, D. Chanda, Y. Huang, Y. Zhang, J. A. Rogers, *Proc. Natl. Acad. Sci. USA* **2019**, *116*, 13239.
[51] F. Liu, Y. Chen, H. Song, F. Zhang, Z. Fan, Y. Liu, X. Feng, J. A. Rogers, Y. Huang, Y. Zhang, F. F. Electronics Liu, H. Song, F. Zhang, Z. Fan, Y. Liu, X. Feng, Y. Zhang, Y. Chen, J. A. Rogers, Y. Huang, *Small* **2019**, *15*, 1804055.
[52] T. A. Truong, T. K. Nguyen, H. Zhao, N. K. Nguyen, T. Dinh, Y. Park, T. Nguyen, Y. Yamauchi, N. T. Nguyen, H. P. Phan, *Small* **2022**, *18*, 2105748.
[53] S. Sarva, S. Nemat-Nasser, *Mater. Sci. Eng. A* **2001**, *317*, 140.
[54] K. M. Jackson, J. Dunning, C. A. Zorman, M. Mehregany, W. N. Sharpe, *J. Microelectromech. Syst.* **2005**, *14*, 664.
[55] Y. Zhang, Z. Yan, K. Nan, D. Xiao, Y. Liu, H. Luan, H. Fu, X. Wang, Q. Yang, J. Wang, W. Ren, H. Si, F. Liu, L. Yang, H. Li, J. Wang, X. Guo, H. Luo, L. Wang, Y. Huang, J. A. Rogers, *Proc. Natl. Acad. Sci. USA* **2015**, *112*, 11757.
[56] S. A. Hesse, K. E. Fritz, P. A. Beaucage, R. P. Thedford, F. Yu, F. J. Disalvo, J. Suntivich, U. Wiesner, *ACS Nano* **2020**, *14*, 16897.